period of 7 days (Fig. 1C). IFN-α and -β both, but the latter more actively, decreased cell proliferation time-dependently at a concentration of 1,000 IU/ml, supporting the previous studies (Mallat et al., 1995; Shen et al., 2002). Dose-dependency of the growth inhibition is shown in IFN concentrations from 10 to 1,000 IU/ml (Fig. 1D).

Effects of IFN-α and -β on cell cycle distribution

To elucidate the mechanism of the growth inhibitory effect of IFN, we next examined the change in cell cycle distribution in response to IFN-α and -β treatment by flow cytometry. LX-2 cells were synchronized in G0/G1 phase by serum starvation for 24 h. In non-treated cells (control), population in G0/G1 phase was reduced after serum exposure, which was accompanied by the increase of population in S phase. This cell cycle transition peaked at 24 h (Fig. 2, upper part). In cells treated with IFN-α or -β, the G0/G1 phase population was larger and the S phase population was smaller than in the control cells at 15 h and 24 h. In addition, the accumulation of cells in early S phase was observed at 32–48 h (Fig. 2, middle and lower parts). These delays in cell cycle shift were more potent in IFN-β-treated cells than in IFN-α-treated cells. It was concluded that type I IFN hampered HSC proliferation through a delay in the cell cycle at the transition from G1 to S phase and in the progression of S phase.

Regulation of cyclin E1 and p21 expression by IFN-β

IFN-β was chosen in the following experiments because of its more potent inhibition of cell cycle progression than IFN-α as described above. The transition from G1 to S phase and the progression of S phase are known to be influenced by various regulators (Golias et al., 2004). Among them, we found that IFN-β significantly decreased cyclin E1 mRNA expression levels by 0.6- to 0.7-fold at 6 and 24 h and increased p21 mRNA expression levels by 1.4- to 2.3-fold at 6, 24, 48, and 72 h in LX-2 cells (Fig. 3). The expression levels of CDK4 and CDK6 were also reduced by IFN-β at early phase with less extent. The others showed negligible change within 24 h although variable dynamics were seen thereafter; changes of cyclin D1, CDK2, and p27 expression at late phase were toward cell cycle promotion with currently unknown reason.

Regulation of miR-195 expression by IFN-β

The result indicated from Figure 1 strongly suggested the possibility that IFN-β increase the expression of miR-195 in LX-2 cells. To test this possibility, we examined the expression levels of miR-195 in IFN-β-treated LX-2 cells. As a result, the miR-195 expression level was significantly increased by IFN-β treatment at 24, 48, and 72 h (Fig. 4A).

Regulation of cyclin E1 and p21 expression by miR-195

The results obtained from experiments shown in Figures 3 and 4A led us to hypothesize that IFN-β up-regulates the expression of miR-195, which then down-regulates the expression of cyclin E1 and up-regulates the expression of p21. In addition, there had been a study reporting that miR-195 targets E2F3, CDK6, and cyclin D1 in addition to cyclin E1 (Xu et al., 2009). Under these considerations, we examined the changes in the expression levels of the above-mentioned cell cycle-related molecules and CDK4 by introducing miR-195

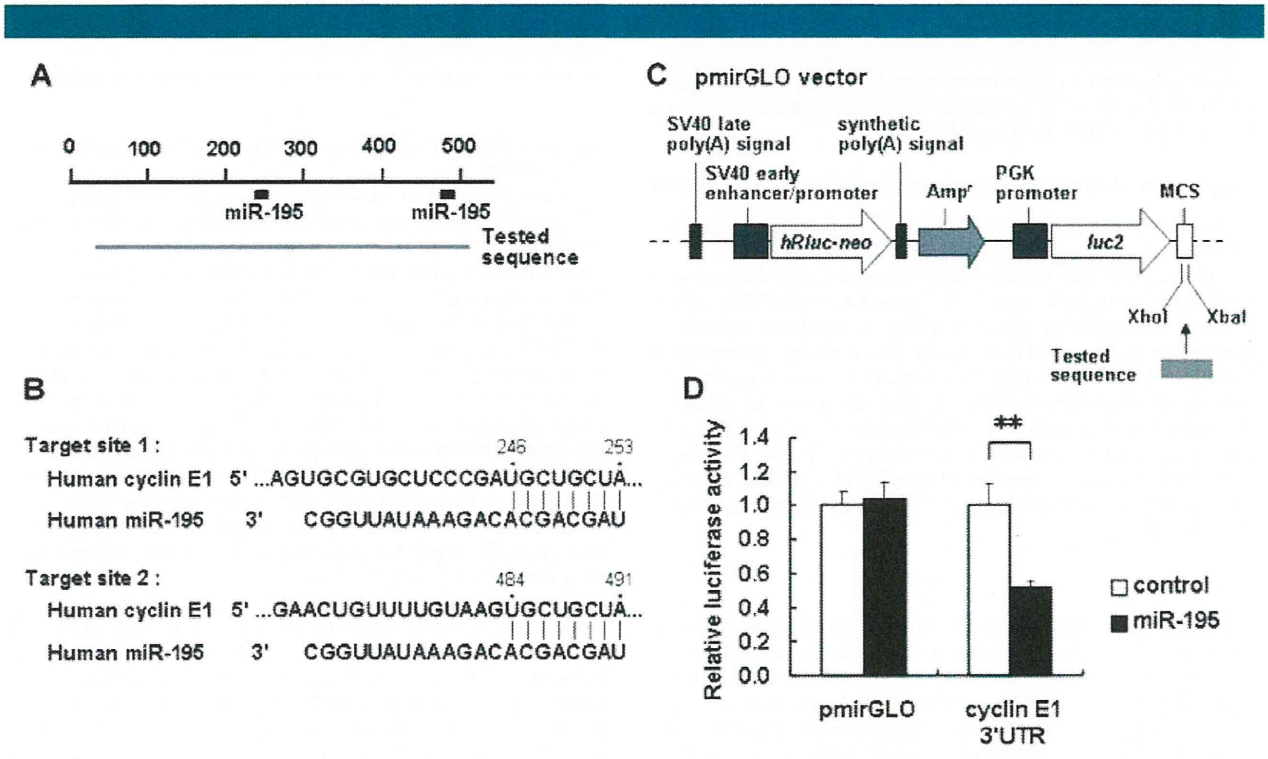

Fig. 5. Interaction of miR-195 with the 3′UTR of cyclin E1 mRNA. A: Schematic indication of the putative miR-195 target sites in the 3′UTR of the cyclin E1 mRNA. Tested sequences indicate the regions that were inserted into the luciferase reporter vector. **B:** Predicted pairing of the target region and miRNAs. **C:** Structure of the luciferase reporter vector (Ogawa et al., 2010). The putative miR-195 target region in cyclin E1 3′UTR (tested sequence) was ligated into the MCS. Arrows indicate the gene directions. Amp^R indicates an ampicillin resistance gene. **D:** Reporter gene assay of the interaction between the 3′UTR of cyclin E1 mRNA and miR-195 in LX-2 cells. Results are expressed as the relative activities against the activity in the presence of the control. $^*P < 0.05$, $^{**}P < 0.01$ compared with control.

precursor into LX-2 cells. Transfection of miR-195 precursor increased the miR-195 expression levels in LX-2 cells by up to 10,000–30,000 times compared with those in cells transfected with negative control (data not shown). Cyclin E1 mRNA and protein expression levels showed a remarkable reduction up to 72 h as result of miR-195 overexpression (Fig. 4B,C). On the other hand, p21 mRNA and protein expression levels showed a marked increase. CDK4, CDK6, and cyclin D1 expression levels were significantly changed at the mRNA level, but negligibly at the protein level. E2F3 mRNA and protein expression levels were unchanged (Fig. 4B,C). These results suggested that miR-195 mainly regulated cyclin E1 and p21 expression in LX-2 cells. Moreover, transfection of miR-195 precursor (50 nM) decreased the proliferation of LX-2 cells in the WST-1 assay (Fig. 4D). These results showed that miR-195 down-regulates endogenous cyclin E1 expression and up-regulates p21 expression, resulting in the attenuation of cell cycle progression and cell proliferation.

Interaction of miR-195 with cyclin E1 3′UTR in LX-2 cells

Next, we examined whether miR-195 interacted directly with cyclin E1 3′UTR in LX-2 cells. The predicted miRNA target sites for miR-195 in the cyclin E1 3′UTR were analyzed using TargetScan Human Release 5.1 (http://www.targetscan.org/). The cyclin E1 3′UTR contained two target sites for miR-195 (Fig. 5A,B). To investigate the direct interaction between them, the part of the cyclin E1 3′UTR containing the two miR-195 target sites (497 bp) was cloned from LX-2 cells, inserted the downstream of a firefly luciferase reporter gene in a pmirGLO vector (Fig. 5C), and cotransfected into LX-2 cells. As shown in Figure 5D, luciferase reporter activity decreased significantly in miR-195 precursor-transfected cells compared with cells transfected with a negative control of the precursor. These results suggested a direct interaction between miR-195 and cyclin E1 3′UTR in LX-2 cells. Binding site of miR-195 was not found in p21 3′UTR by TargetScan.

Regulation of cyclin E1 expression by IFN-β and miR-195

To confirm the contribution of miR-195 to the inhibitory effect of IFN-β on cyclin E1 expression, LX-2 cells were first transfected with 50 nM miR-195 inhibitor and then treated with 1,000 IU/ml IFN-β. As shown in Figure 6A, miR-195 inhibitor blocked the inhibitory effect of IFN-β on cyclin E1 mRNA expression at 16 and 24 h. Although there was no difference in the cyclin E1 mRNA expression between IFN-β-treated cells and non-treated cells (control) at 48 h, the cyclin E1 mRNA expression level in miR-195 inhibitor plus IFN-β-treated cells was up-regulated compared with non-treated cells (Fig. 6A). Immunoblot analysis revealed that miR-195 inhibitor elevated the cyclin E1 expression level of IFN-β-treated cells at 24 and 48 h (Fig. 6B).

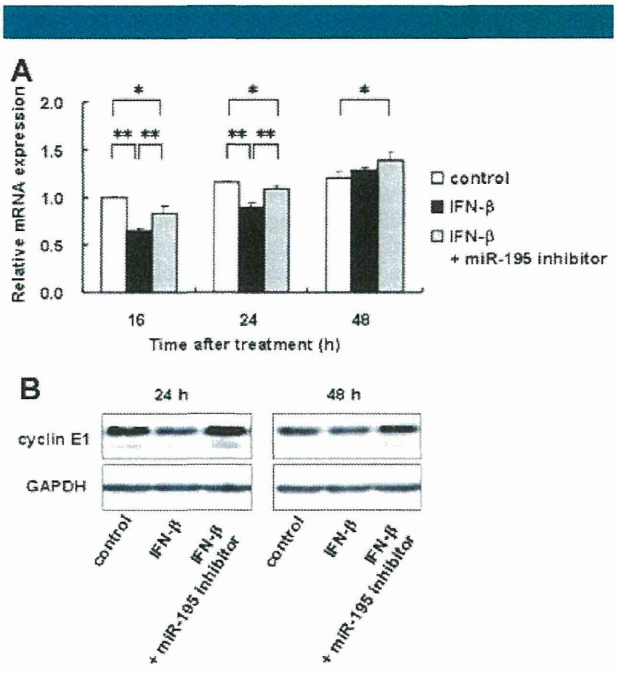

Fig. 6. Regulation of cyclin E1 expression by IFN-β and miR-195. LX-2 cells were transfected with 50 nM miR-195 inhibitor or a negative control. After 6 h, the culture medium was changed and then IFN-β (1,000 IU/ml) was added. Cells were then incubated for the indicated time periods. A: mRNA expression levels of cyclin E1. B: Protein expression levels of cyclin E1. GAPDH are for loading adjustment. Control; cells were transfected with a negative control and incubated without IFN-β. *$P < 0.05$, **$P < 0.01$.

Discussion

In this study, we showed that IFN-β is more antiproliferative on LX-2 cells than IFN-α, which appears to be contradictory to their known mechanism of action: both IFN-α and -β exert their activities through the common signaling pathway, beginning with binding to the same type I IFN receptor (IFNAR) consisting of IFNAR1 and IFNAR2, which activate the common components of janus kinase/signal transducer and activator of transcription (STAT) pathway (Darnell et al., 1994). However, a similar activity difference between the IFNs has also been demonstrated in colon cancer cell lines (Katayama et al., 2007) and in rat HSCs (Shen et al., 2002). Some studies showed that IFN-β but not IFN-α formed a stable complex with IFNARs, suggesting that IFN-β may interact with IFNAR chains in a manner different from IFN-α (Croze et al., 1996; Russell-Harde et al., 1999).

We showed here that IFN-β down-regulated the expression of cyclin E1 and up-regulated the expression of p21, which caused the cells to be less active proceeding in the transition from G0 to G1 phase and in the progression of S phase. The cell cycle is regulated by various molecules, such as cyclins and CDKs. Cyclin E is essential in activating CDK2. The cyclin E-CDK2 complex phosphorylates pRb at G1 phase, leading to gene transcription activities that are needed in S phase, and also activates the factors involved in DNA replication at early S phase (Golias et al., 2004). It has been reported that cyclin E1 expression increased in non-parenchymal cells of human fibrotic liver and that cyclin E1-deficient mice developed milder liver fibrosis compared with wild-type mice after CCl_4 administration (Nevzorova et al., 2010). These results imply that cyclin E1 regulates the progression of liver fibrosis by accelerating HSC proliferation.

The most frequent miRNAs that targets cyclin E1 are the miR-16 family, which consists of miR-15, -16, -195, -424, and -497 (Liu et al., 2008; Wang et al., 2009). We here observed the induction of miR-195 by IFN-β. miR-195 was reported to be down-regulated in human HCC tissues and to suppress HCC growth through the targeted interference of cyclin D1, CDK6, and E2F3 in a *xenograft* mouse model (Xu et al., 2009), while it was reported to target cyclin E1 in addition to the above-mentioned factors in A549 cells (Liu et al., 2008). miR-15b and miR-16 are down-regulated concomitantly with HSC activation and their overexpression induces apoptosis and a delay of cell cycle in HSCs by targeting Bcl-2 and cyclin D1 (Guo et al., 2009a,b). However, the role of miR-195 in HSCs remains unknown. We showed here that miR-195 expression was

decreased during spontaneous activation of primary-cultured mouse HSCs and that miR-195 interacted with cyclin E1 3′UTR and lowered the expression levels of the cyclin E1 mRNA and protein in LX-2 cells. These results suggest that the down-regulation of miR-195 may associate with the proliferation of HSCs in fibrotic liver similarly to miR-15 and miR-16. In this study, the changes of the protein expression levels of E2F3, CDK6, and cyclin D1, which were reported to be regulated by miR-195 (Xu et al., 2009), were negligible by miR-195, although the exact reason for this phenomenon was not determined. However, because the total context scores obtained by TargetScan were −0.73 for cyclin E1, −0.33 for E2F3, −0.32 for cyclin D1, and −0.09 for CDK6, the result obtained here was thought to be reasonable. In addition, minimal or negligible effect of miR-195 on the expression of E2F3, CDK4, CDK6, and cyclin D1 was compatible with that of IFN-β on these factors. Furthermore, inhibition of miR-195 by miR-195 inhibitor attenuated the effect of IFN-β on cyclin E1 expression, though not so strong. Taken together, it is most likely that the down-regulation of cyclin E1 by IFN-β treatment in HSCs is mediated through miR-195 up-regulation. The mechanism through which IFN-β induces miR-195 in LX-2 cells need to be explored further.

It is well known that IFNs induce the expression of p21 in various cancer cells (Sangfelt et al., 1999; Katayama et al., 2007). We also observed the up-regulation of p21 in IFN-β-treated cells. Therefore, p21, in addition to cyclin E1, may play a role in IFN-induced growth inhibition of HSCs. Until now, it has been reported that IFNs induce p21 expression through the binding of STAT and IFN regulatory factor, which are critical signaling molecules after IFN-IFNAR interaction, to p21 gene promoter (Gartel and Tyner, 1999). Unexpectedly, we found the up-regulation of p21 by miR-195 (Fig. 4). The results obtained here raise a new possibility that the up-regulation of p21 by IFN-β in HSCs may be partially mediated through miR-195.

In conclusion, type I IFN, in particular IFN-β, inhibited the proliferation of human HSCs by delaying the cell cycle in G1 to early S phase through the down-regulation of cyclin E1 and up-regulation of p21. The cyclin E1 down-regulation and p21 up-regulation were partially mediated by miR-195 that was up-regulated by IFN-β. This study raises a new mechanistic aspect of the antifibrotic effect of IFN in liver fibrosis and the possibility of influencing miR-195 as a therapeutic strategy for liver fibrosis.

Acknowledgments

This work was supported by a grant from the Ministry of Health, Labour and Welfare of Japan to N. Kawada (2008–2010).

Literature Cited

Bartel DP. 2004. MicroRNAs: Genomics, biogenesis, mechanism, and function. Cell 116:281–297.

Bataller R, Brenner DA. 2001. Hepatic stellate cells as a target for the treatment of liver fibrosis. Semin Liv Dis 21:437–451.

Chang XM, Chang Y, Jia A. 2005. Effects of interferon-alpha on expression of hepatic stellate cell and transforming growth factor-beta1 and alpha-smooth muscle actin in rats with hepatic fibrosis. World J Gastroenterol 11:2634–2636.

Croze E, Russell-Harde D, Wagner TC, Pu H, Pfeffer LM, Perez HD. 1996. The human type I interferon receptor. Identification of the interferon beta-specific receptor-associated phosphoprotein. J Biol Chem 271:33165–33168.

Darnell JE, Kerr IM, Stark GR. 1994. Jak-STAT pathways and transcriptional activation in response to IFNs and other extracellular signaling proteins. Science 264:1415–1421.

Fort J, Pilette C, Veal N, Oberti F, Gallois Y, Douay O, Rosenbaum J, Cales P. 1998. Effects of long-term administration of interferon alpha in two models of liver fibrosis in rats. J Hepatol 29:263–270.

Friedman SL. 2000. Molecular regulation of hepatic fibrosis, an integrated cellular response to tissue injury. J Biol Chem 275:2247–2250.

Gartel AL, Tyner AL. 1999. Transcriptional regulation of the p21(WAF1/CIP1) gene. Exp Cell Res 246:280–289.

Golias CH, Charalabopoulos A, Charalabopoulos K. 2004. Cell proliferation and cell cycle control: A mini review. Int J Clin Pract 58:1134–1141.

Guo CJ, Pan Q, Jiang B, Chen GY, Li DG. 2009a. Effects of upregulated expression of microRNA-16 on biological properties of culture-activated hepatic stellate cells. Apoptosis 14:1331–1340.

Guo CJ, Pan Q, Li DG, Sun H, Liu BW. 2009b. miR-15b and miR-16 are implicated in activation of the rat hepatic stellate cell: An essential role for apoptosis. J Hepatol 50:766–778.

Inagaki Y, Nemoto T, Kushida M, Meng Y, Higashi K, Ikeda K, Kawada N, Shirasaki F, Takehara K, Sugiyama K, Fujii M, Yamauchi H, Nakao A, de Crombrugghe B, Watanabe T, Okazaki I. 2003. Interferon alpha down-regulates collagen gene transcription and suppresses experimental hepatic fibrosis in mice. Hepatology 38:890–899.

Ji JF, Shi J, Budhu A, Yu ZP, Forgues M, Roessler S, Ambs S, Chen YD, Meltzer PS, Croce CM, Qin LX, Man K, Lo CM, Lee J, Ng IOL, Fan J, Tang ZY, Sun HC, Wang XW. 2009a. MicroRNA expression, survival, and response to interferon in liver cancer. N Engl J Med 361:1437–1447.

Ji JL, Zhang JS, Huang GC, Qian J, Wang XQ, Mei S. 2009b. Over-expressed microRNA-27a and 27b influence fat accumulation and cell proliferation during rat hepatic stellate cell activation. FEBS Lett 583:759–766.

Katayama T, Nakanishi K, Nishihara H, Kamiyama N, Nakagawa T, Kamiyama T, Iseki K, Tanaka S, Todo S. 2007. Type I interferon prolongs cell cycle progression via p21(WAF1/CIP1) induction in human colon cancer cells. Int J Oncol 31:613–620.

Liu Q, Fu HJ, Sun F, Zhang HM, Tie Y, Zhu J, Xing RY, Sun ZX, Zheng XF. 2008. miR-16 family induces cell cycle arrest by regulating multiple cell cycle genes. Nucleic Acids Res 36:5391–5404.

Mallat A, Preaux AM, Blazejewski S, Rosenbaum J, Dhumeaux D, Mavier P. 1995. Interferon alpha and gamma inhibit proliferation and collagen synthesis of human Ito cells in culture. Hepatology 21:1003–1010.

Nevzorova YA, Bangen JM, Gassler N, Haas U, Weiskirchen R, Tacke F, Sicinski P, Trautwein C, Liedtke C. 2010. Cyclin E1 controls the cell cycle activity of hepatic stellate cells and triggers fibrogenesis in mice. J Hepatol 52:S374–S375.

Ogawa T, Kawada N, Ikeda K. 2009. Effect of natural interferon alpha on proliferation and apoptosis of hepatic stellate cells. Hepatol Int 3:497–503.

Ogawa T, Iizuka M, Sekiya Y, Yoshizato K, Ikeda K, Kawada N. 2010. Suppression of type I collagen production by microRNA-29b in cultured human stellate cells. Biochem Biophys Res Commun 391:316–321.

Pedersen IM, Cheng G, Wieland S, Volinia S, Croce CM, Chisari FV, David M. 2007. Interferon modulation of cellular microRNAs as an antiviral mechanism. Nature 449:919–922.

Pestka S, Langer JA, Zoon KC, Samuel CE. 1987. Interferons and their actions. Annu Rev Biochem 56:727–777.

Russell-Harde D, Wagner TC, Perez HD, Croze E. 1999. Formation of a uniquely stable type I interferon receptor complex by interferon beta is dependent upon particular interactions between interferon beta and its receptor and independent of tyrosine phosphorylation. Biochem Biophys Res Commun 255:539–544.

Sangfelt O, Erickson S, Castro J, Heiden T, Gustafsson A, Einhorn S, Grander D. 1999. Molecular mechanisms underlying interferon-alpha-induced G0/G1 arrest: CKI-mediated regulation of G1 Cdk-complexes and activation of pocket proteins. Oncogene 18:2798–2810.

Shen H, Zhang M, Minuk GY, Gong YW. 2002. Different effects of rat interferon alpha, beta and gamma on rat hepatic stellate cell proliferation and activation. BMC Cell Biol 3:9.

Tanabe J, Izawa A, Takemi N, Miyauchi Y, Torii Y, Tsuchiyama H, Suzuki T, Sone S, Ando K. 2007. Interferon-beta reduces the mouse liver fibrosis induced by repeated administration of concanavalin A via the direct and indirect effects. Immunology 122:562–570.

Uyama N, Zhao L, Van Rossen E, Hirako Y, Reynaert H, Adams DH, Xue Z, Li Z, Robson R, Pekny M, Geerts A. 2006. Hepatic stellate cells express synemin, a protein bridging intermediate filaments to focal adhesions. Gut 55:1276–1289.

Uze G, Schreiber G, Piehler J, Pellegrini S. 2007. The receptor of the type I interferon family. Curr Top Microbiol Immunol 316:71–95.

Venugopal SK, Jiang J, Kim TH, Li Y, Wang SS, Torok NJ, Wu J, Zern MA. 2010. Liver fibrosis causes downregulation of miRNA-150 and miRNA-194 in hepatic stellate cells, and their overexpression causes decreased stellate cell activation. Am J Physiol Gastrointest Liver Physiol 298:G101–G106.

Wang F, Fu XD, Zhou Y, Zhang Y. 2009. Down-regulation of the cyclin E1 oncogene expression by microRNA-16-1 induces cell cycle arrest in human cancer cells. BMB Rep 42:725–730.

Xu L, Hui AY, Albanis E, Arthur MJ, O'Byrne SM, Blaner WS, Mukherjee P, Friedman SL, Eng FJ. 2005. Human hepatic stellate cell lines, LX-1 and LX-2: New tools for analysis of hepatic fibrosis. Gut 54:142–151.

Xu T, Zhu Y, Xiong YJ, Ge YY, Yun JP, Zhuang SM. 2009. MicroRNA-195 suppresses tumorigenicity and regulates G(1)/S transition of human hepatocellular carcinoma cells. Hepatology 50:113–121.

The American Journal of Pathology, Vol. 179, No. 2, August 2011

DOI: 10.1016/j.ajpath.2011.05.006

Tumorigenesis and Neoplastic Progression

Promotion of Liver and Lung Tumorigenesis in DEN-Treated Cytoglobin-Deficient Mice

Le Thi Thanh Thuy,*† Takashi Morita,‡ Kayo Yoshida,‡ Kenichi Wakasa,§ Masashi Iizuka,*† Tomohiro Ogawa,*† Mami Mori,* Yumiko Sekiya,*† Shinobu Momen,*† Hiroyuki Motoyama,* Kazuo Ikeda,¶ Katsutoshi Yoshizato,*†‖ and Norifumi Kawada*†

From the Departments of Hepatology, Molecular Genetics,‡ and Diagnostic Pathology,§ and the Liver Research Center,† Graduate School of Medicine, Osaka City University, Osaka; the Department of Anatomy and Cell Biology,¶ Graduate School of Medical Sciences, Nagoya City University, Aichi; and the Academic Advisor's Office, PhoenixBio Co., Ltd., Hiroshima, Japan*

Cytoglobin (Cygb) is a recently discovered vertebrate globin with molecular characteristics that are similar to myoglobin. To study the biological function of Cygb *in vivo*, we generated *Cygb* knockout mice and investigated their susceptibility to *N*,*N*-diethylnitrosamine (DEN)–induced tumorigenesis. Four-week-old male mice were administered DEN in drinking water at a dose of 25 ppm for 25 weeks or 0.05 ppm for 36 weeks. *Cygb* deficiency promoted the DEN-induced development of liver and lung tumors. All $Cygb^{+/-}$ and $Cygb^{-/-}$ mice treated with 25-ppm DEN exhibited liver tumors, compared with 44.4% of their wild-type counterparts. Lung tumors were present only in *Cygb*-deficient mice. More than 40% of $Cygb^{-/-}$ mice developed liver and lung tumors at the nontoxic dose of DEN (0.05 ppm), which did not induce tumors in wild-type mice. *Cygb* loss was associated with increased cancer cell proliferation, elevated extracellular signal–regulated kinase and Akt activation, overexpression of IL-1β, IL-6, Tnfα, and Tgfβ3 mRNAs, and hepatic collagen accumulation. *Cygb*-deficient mice also exhibited increased nitrotyrosine formation and dysregulated expression of cancer-related genes (cyclin D2, p53, Pak1, Src, Cdkn2a, and Cebpa). These results suggest that *Cygb* deficiency induces susceptibility to cancer development in the liver and lungs of mice exposed to DEN. Thus, globins such as Cygb will shed new light on the biological features of organ carcinogenesis. *(Am J Pathol 2011, 179:1050–1060; DOI: 10.1016/j.ajpath.2011.05.006)*

Cytoglobin (Cygb) was originally identified in 2001 as a protein up-regulated in rat hepatic stellate cells under profibrotic conditions. Accordingly, Cygb was originally termed a stellate cell activation-associated protein[1] until it was identified as the fourth globin in mammals.[2,3] Human Cygb displays approximately 25% amino acid identity with vertebrate myoglobin and hemoglobin and 16% identity with human neuroglobin. The *Cygb* gene is localized to chromosome 17q25.3 in humans and chromosome 11E2 in mice.

Unlike myoglobin, which is tissue restricted to cardiomyocytes and skeletal myofibers, hemoglobin in erythrocytes, and neuroglobin in the nervous system, Cygb is ubiquitously expressed in the cytoplasm of mesenchymal fibroblastic cells in many organs, including the heart, lung, liver, kidneys, small intestine, and spleen. The presence of Cygb in the nucleus of these cells has also been reported.[4,5] In particular, Cygb was present in stellate cells and myofibroblasts in the liver and pancreas, reticulocytes in the spleen, mesenchymal cells in the submucosal layer of the gut, and the mesangium and stromal cells of the kidney.[4] An interesting aspect of Cygb expression is its presence in visceral cells, with a strong storage ability for vitamin A. Thus, Cygb may facilitate the diffusion of oxygen through tissues, scavenge nitric oxide (NO) or other reactive oxygen species, or serve a protective function during oxidative stress.[6] However, the precise physiological role of Cygb *in vivo* remains unresolved. Cygb is considered a hypoxia-responsive molecule because its mRNA expression is augmented under hypoxia in fibroblastic cell lineages and rat brain.[7] Hypoxia-inducible factor 1 is assumed to be an important transcription factor for *Cygb* because hypoxia-responsive elements at positions -141, -144, and -448 are essential for the acti-

Supported by a Grant-in-Aid for Scientific Research from the Japan Society for the Promotion of Science [grant 21390232 (2009) to N.K.]; grants from the Ministry of Health, Labour, and Welfare of Japan (2008); and the Thrust Area Research grant from Osaka City University (2008).

Accepted for publication May 2, 2011.

Presented in part at the 16th International Symposium on Cells of the Hepatic Sinusoid, Pasadena, CA, September 2, 2010.

Address reprint requests to Norifumi Kawada, M.D., Ph.D., Department of Hepatology, Graduate School of Medicine, Osaka City University, 1-4-3 Asahimachi, Abeno, Osaka 545-8585, Japan. E-mail: kawadanori@med.osaka-cu.ac.jp.

vation of CYGB gene expression, and the binding of hypoxia-inducible factor 1 to this area has been confirmed.[8,9] In contrast, CYGB overexpression rescues the human neuronal cell line TE671 from prooxidant Ro19-8022–induced DNA damage.[10] CYGB overexpression also protected human neuroblastoma SH-SY5Y cells from H_2O_2-induced cell death.[11,12] Furthermore, the *in vitro* and *in vivo* overexpression of Cygb in rat hepatic stellate cells protected these cells against oxidative stress and inhibited their differentiation into an active phenotype.[13] Together, these reports suggest that Cygb may act as a cytoprotective and radical-scavenging molecule in addition to its function as a gas carrier.

Although the function of Cygb *in vivo* remains largely unknown, down-regulation of CYGB has been reported in several human cancerous tissues and human cancer cell lines. Decreased expression of CYGB and the hypermethylation of the CYGB promoter has been reported in patients with tylosis, non–small-cell lung carcinoma tissues, head and neck cancers, ovarian cancers, and breast cancers.[14–18] McRonald et al[14] reported that CYGB gene expression in tylosis with esophagus cancer was reduced to approximately 70% compared with the normal esophagus and was accompanied by hypermethylation of the promoter. Xinarianos et al[15] reported a significant reduction of CYGB mRNA expression in non-small-cell lung carcinoma tissues and hypermethylation of CYGB, compared with healthy samples. Similar results were reported in head and neck, ovarian, and breast cancer tissues.[16–18] In addition, Shivapurkar et al[19] reported high levels of CYGB promoter methylation in lung, breast, bladder, and colon cancers and in leukemia in humans. The augmented growth of NCI-H661 lung cancer cells that were CYGB silenced by RNA interference and the suppression of NCI-H228 cell proliferation in cells stably transfected with plasmids containing CYGB cDNA have also been reported.[19] These reports indicate a tumor suppressor function of *Cygb*.

To study the biological function of *Cygb* at the tissue level, we first generated *Cygb*-deficient ($Cygb^{-/-}$) mice and observed that, after treatment with *N,N*-diethylnitrosamine (DEN), $Cygb^{-/-}$ mice showed a high incidence of tumor development in the liver and lungs. These results indicate the tumor suppressor role of *Cygb in vivo*.

Materials and Methods

Materials

All experimental reagents were obtained from Sigma Chemical Co (St. Louis, MO) or Wako Pure Chemical Co (Osaka, Japan), unless otherwise stated.

Construction of the Targeting Vector

Mice lacking exon 1 of the *Cygb* gene were generated using the lox-P system, as previously described.[20] The targeting vector (pTVneo/*Cygb*) was constructed from PCR DNA fragments from 129Sv mouse genomic DNA. Two DNA fragments were used as the 3′ and 5′ arms. One fragment contained *Cygb* exons 2, 3, and 4 (6.5 kb); and the other contained the transcription initiation site in exon 1 and the 5′ upstream sequence of the *Cygb* gene (6.0 kb). The neomycin-resistance gene, driven by the phosphoglycerate kinase 1 promoter, flanking the lox-P sequences was inserted into the arms (Figure 1A).

Embryonic stem cells (1×10^7 cells/mL) were transfected with a linearized targeting vector (20 μg) by electroporation and cultured in selection medium containing 150 μg/mL geneticine (G418). Of 480 neomycin-resistant clones, 6 (1.2%) were homologous recombinants by Southern blotting using the 5′ probe (data not shown).

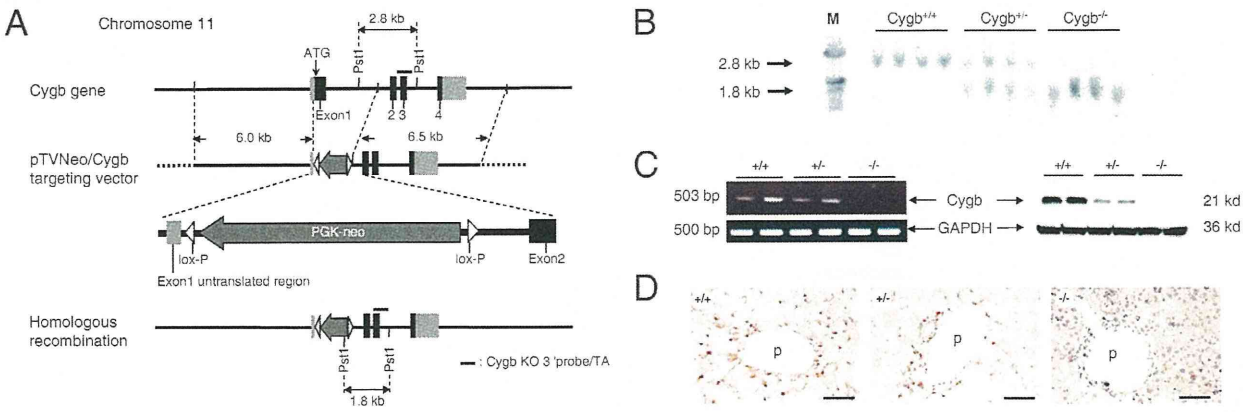

Figure 1. Generation of *Cygb*-deficient mice. **A:** Strategy for inactivation of the *Cygb* gene by homologous recombination in embryonic stem cells. A partial genomic map of the *Cygb* gene with coding exons (**black boxes**), noncoding regions (**light gray boxes**), and flanking introns (**solid lines**) is shown (**top**). Targeting vector pTVneo/*Cygb* with homology to the *Cygb* gene locus is shown (**middle**). The translation initiation site in exon 1 was replaced with a neomycin-resistance cassette. The predicted *Cygb* gene locus after homologous recombination is shown (**bottom**). **B:** Southern blot analysis shows the sizes of the wild-type (2.8-kb) and disrupted (1.8-kb) *Cygb* fragments after PstI cleavage. M, molecular weight marker. **C:** RT-PCR and immunoblot analysis of Cygb expression in the liver from $Cygb^{+/+}$, $Cygb^{+/-}$, and $Cygb^{-/-}$ mice. GAPDH was used as a loading control. **D:** Representative IHC images of Cygb in the liver of $Cygb^{+/+}$, $Cygb^{+/-}$, and $Cygb^{-/-}$ mice. Cygb is present along the sinusoids of $Cygb^{+/+}$ mice, whereas it is undetectable in $Cygb^{-/-}$ mice. p, portal vein. Scale bar = 50 μm.

Production of Cygb-*Deficient Mice*

Two clones were aggregated with C57BL/6-DBA2 F1 mouse morulae, and one produced chimeric mice that transmitted the knockout (KO) construct. Chimeric males were mated with C57BL/6J females to obtain *Cygb* heterozygous mice that were backcrossed to the C57BL/6J background for more than nine generations. To assess the role of the *Cygb* gene in development, we intercrossed *Cygb* heterozygous mice. The litter sizes were normal, and analysis of the tail biopsy specimens at the age of 4 weeks, from 102 offspring from heterozygote crosses, revealed the presence of homozygous mutant mice at a frequency of 24%. The homozygotes appeared normal morphologically and histopathologically 1 month after birth. Four-week-old $Cygb^{+/+}$ (wild-type), $Cygb^{+/-}$ (heterozygote), and $Cygb^{-/-}$ (homozygote) male mice were used in this study.

All mice were cared for according to the guidelines approved by the Institutional Animal Care and Use Committee of Osaka City University, Osaka.

Genotyping of Mice

PCR genotyping of mouse tail DNA produced the expected 338-bp product from wild-type mice using the following primer pairs: forward, 5′-CTCCCAGCCGGGACCGCGGTGGCCTT-3′; and reverse, 5′-GGAGCCGAGGCCGGTGCGTGCGAGGC-3′. A 529-bp product was diagnostic for the *Cygb* KO allele using the described forward primer and the following reverse primer: 5′-GTGGGGTGGGATTAGATAAATGCCTGCTCT-3′. PCR was performed in a 15-μL reaction mixture containing 1 μL of extract from mouse tail DNA, which was digestion extracted using LYPPO (Gene Modification R&D Co Ltd, Osaka), according to the manufacturer's protocol; 1 μmol/L of each primer; 2.5% to 5% dimethyl sulfoxide; and 0.5 U GO Taq polymerase (Promega, San Luis Obispo, CA). PCRs were performed for 40 cycles, each cycle being 1 minute at 94°C, 30 seconds at 70°C, and 1 minute at 72°C.

Southern blot analysis confirmed the *Cygb*-null allele. Genomic tail DNA (5 μg) was cleaved with PstI, subjected to agarose gel electrophoresis, blotted onto nylon membranes, and hybridized to the ^{32}P-labeled *Cygb* KO 3′ probe/TA (Figure 1A). DNA fragments of 2.8 and 1.8 kb represented the *Cygb* wild-type and null alleles, respectively.

RT-PCR was performed to confirm the absence of Cygb mRNA in tissues. Total RNA was extracted from the homogenates of liver tissues using the RNeasy Mini Kit (Qiagen, Valencia, CA). cDNA was synthesized using 1 μg of total RNA, ReverTra Ace (Toyobo, Osaka), and oligo $(dT)_{12-18}$ primers, according to the manufacturer's instructions. Thirty-five PCR cycles (30 seconds at 94°C, 30 seconds at 68°C, and 1 minute at 72°C) were run using the following mouse Cygb primers: forward, 5′-GCGACATGGAGATAGAGCGT-3′; and reverse, 5′-CTGTACCCAGCCCACTTCCT-3′. This generated a 503-bp product and glyceraldehyde-3-phosphate dehydrogenase (GAPDH) primers: forward, 5′-CGCCTGGTCACCAGG-3′; and reverse, 5′-CAGTTGGTGGTGCAGGA-3′). A 500-bp product was generated.

Administration of DEN

DEN (0.95 g/mL) was obtained from Sigma Chemical Co. A stock solution of DEN was prepared by dissolving 1 g (1.06 mL) of DEN in 400 mL of water. The stock solution was diluted 100-fold before use to obtain a final concentration of 25-mg DEN per 1000-mL water (25 ppm) for the high-dose experiment. The 25-ppm solution was further diluted 500-fold to obtain a final concentration of 0.05-mg DEN per 1000-mL water (0.05 ppm) for the low-dose experiment. The diluted solution (25 or 0.05 ppm) was placed in a shaded serving bottle and administered to the animals instead of water. The diluted solution was prepared weekly. The administration of DEN to male mice began at the age of 4 weeks for 25 weeks in the high-dose experiment (25 ppm) and for 36 weeks in the low-dose experiment (0.05 ppm). Each experiment contained three groups ($Cygb^{+/+}$, $Cygb^{+/-}$, and $Cygb^{-/-}$) with a

Table 1. Primary Antibodies Used for IHC Analyses

Antigen*	Source	Name/clone; catalog no.	Incubation
AFP	US Biological, Swampscott, MA	F4100-16A (Go)	Overnight 4°C, 1:20
CK19	Santa Cruz Biotechnology, Santa Cruz, CA	Polyclonal (Rb); sc-33111	Overnight 4°C, 1:100
CRBP-1	Santa Cruz Biotechnology	Polyclonal (Rb); sc-30106	Overnight 4°C, 1:100
Cygb	Our laboratory†	Polyclonal (Rb)	Overnight 4°C, 1:100
Erk	Cell Signaling, Danvers, MA	Monoclonal (Rb); 4695	Overnight 4°C, 1:300
PCNA	Dako, Glostrup, Denmark	Monoclonal (Mo)‡; clone: PC-10	Overnight 4°C, 1:200
Phosphorylated Erk	Cell Signaling	Monoclonal (Rb); 4370	Overnight 4°C, 1:200
α-SMA	Dako	Monoclonal (Mo)‡; clone: 1A4	30 minutes at room temperature, 1:100
Desmin	Santa Cruz Biotechnology	Polyclonal (Go); sc-7559	Overnight 4°C, 1:100

*All antigens were retrieved by autoclaving for 15 minutes in 0.01 mol/L citrate buffer containing 0.05% Tween 20 (pH 6.0), except for desmin, which was used in Tris-EDTA buffer (pH 9.0).
†Data taken from Kawada et al.[1]
‡For mouse primary antibodies, after antigen retrieval, sections were incubated with goat anti-mouse IgG Fab fragments (Jackson ImmunoResearch Laboratories) for 1 hour at room temperature (1:100) to block nonspecific background staining.
AFP, alpha-fetoprotein.

minimum of seven mice per group. Mice were sacrificed after the completion of DEN treatment.

Necropsy

At necropsy, mice were weighed, anesthetized, and examined for grossly visible lesions in whole organs. Livers and lungs were excised, weighed (in the case of liver), and examined for macroscopic lesions. The number of macroscopic abnormal masses ≥1 mm was determined in addition to the size of the mass by taking the average of the largest and smallest length of the mass. For histological examination, 2- to 3-mm-thick sections from nontumor or tumor tissues were fixed in 10% formalin for 24 hours and embedded in paraffin. The samples were then sectioned at 5 μm and stained with H&E.

IHC and TUNEL Assays

For immunohistochemistry (IHC), paraffin sections were dewaxed in xylene and rehydrated in decreasing concentrations of ethanol. The primary antibodies and conditions used for IHC are listed in Table 1. Negative controls with no primary antibody were used to assess nonspecific staining. The secondary antibodies used were horseradish peroxidase–conjugated goat anti-rabbit IgG (1:200; Dako, Glostrup, Denmark), rabbit anti-goat IgG (1:200; Dako), or rabbit anti-mouse IgG (1:200; Dako). 3,3′-Diaminobenzidine (Dako) was used as the chromogen. TdT-mediated dUTP-biotin nick-end labeling (TUNEL) staining was performed using the *In situ* Apoptosis Detection Kit (MK500; TaKaRa Bio Inc., Shiga, Japan), according to the manufacturer's protocol. All sections were counterstained with Meyer's hematoxylin.

Quantification of Liver Fibrosis

Morphometric image analysis was performed in liver tissue specimens with a computerized system, consisting of a photomicroscope, a digital camera, and LuminaVision 2.4 bioimaging software (Mitani Corporation, Tokyo, Japan) to quantitatively assess fibrosis. The proportion of the area stained with Sirius red in the liver sections was calculated as the sum of the pixelwise-bound stain measurements divided by the number of summed pixels.

Quantitative Real-Time PCR

Total RNA was extracted from liver and liver tumor tissues using the RNeasy Mini Kit (Qiagen, Valencia, CA). cDNAs were synthesized as previously described. Gene expression was measured by quantitative real-time PCR using cDNA, real-time PCR Master Mix Reagents (Toyobo, Osaka), or TaqMan Fast Universal PCR Master Mix (Applied Biosystems, Foster City, CA), and a set of gene-specific oligonucleotide primers and probes (Table 2) using an Applied Biosystems Prism 7500 (Applied Biosystems). GAPDH levels were measured and used to normalize the relative abundance of mRNA.

Table 2. Primers Used for RT-qPCR

Gene	Sequence
AFP	
Forward	5′-CACACCCGCTTCCCTCAT-3′
Reverse	5′-TTTTCGTGCAATGCTTTGGA-3′
Bcl2	
Forward	5′-AAGGGCTTCACACCCAAATCT-3′
Reverse	5′-CTTCTACGTCTGCTTGGCTTTGA-3′
Cdkn2a	
Forward	5′-GCTCTGGCTTTCGTGAACATG-3′
Reverse	5′-GTGCGGCCCTCTTCTCAA-3′
Cebpα	
Forward	5′-CGCAAGAGCCGAGATAAAGC-3′
Reverse	5′-CGGTCATTGTCACTGGTCAACT-3′
Col1α1	
Forward	5′-GACATCCCTGAAGTCAGCTGC-3′
Reverse	5′-TCCCTTGGGTCCCTCGAC-3′
Cyclin D1	
Forward	5′-GCCCGGAGGGATTTGC-3′
Reverse	5′-AGACGGAACACTAGAACCTAACAGATT-3′
Cyclin D2	
Forward	5′-AAGGCAGATACTCATCAAACACAGA-3′
Reverse	5′-CTGGTGCACGCATGCAA-3′
Fos	
Forward	5′-CCCCAAACTTCGACCATGAT-3′
Reverse	5′-GGAGGATGACGCCTCGTAGTC-3′
GAPDH	
Forward	5′-TGCACCACCAACTGCTTAG-3′
Reverse	5′-GGATGCAGGGATGATGTTC-3′
IL-6	
Forward	5′-CGCTATGAAGTTCCTCTCTGCAA-3′
Reverse	5′-CACCAGCATCAGTCCCAAGA-3′
IL-1β	
Forward	5′-CCATGGCACATTCTGTTCAAA-3′
Reverse	5′-GCCCATCAGAGGCAAGGA-3′
Jun	
Forward	5′-CCGCCCCTGTCCCCTAT-3′
Reverse	5′-TCCTCATGCGCTTCCTCTCT-3′
Pak1	
Forward	5′-CGTATTGCGGGTGTTTGCTA-3′
Reverse	5′-CACAGCAGGAGAACCAAAACC-3′
p53	
Forward	5′-GCATGAACCGCCGACCTAT-3′
Reverse	5′-CAGAAGGTTCCCACTGGAGTCT-3′
Src	
Forward	5′-CCTCCCGCACCCAGTTC-3′
Reverse	5′-CATCAGCATGTTTGGAGTAGTAAGC-3′
TGFβ3	
Forward	5′-AGGGCCCTGGACACCAATTAC-3′
Reverse	5′-CCTTAGGTTCTGGGACCCATTTC-3′
TNFα	
Forward	5′-CCTCACACTCAGATCTTCTCA-3′
Reverse	5′-GCTGCTCCTCCACTTGGTG-3′
Probe	5′-GCAAGCCTGTAGCCCACGTCGTAGCAAA-3′

Immunoblotting

Protein samples (10 to 20 μg) were subjected to SDS-PAGE and transferred to Immobilon P membranes (Millipore Corp, Bedford, MA). After blocking, membranes were probed with primary antibodies against Cygb (1:500) from our laboratory (Table 1), Akt (1:1000; Cell Signaling, Danvers, MA), phosphorylated Akt (1:500; Cell Signaling), extracellular signal–regulated kinase (Erk; 1:500; Cell Signaling), phosphorylated Erk (1:1000; Cell Signaling), cyclin D1 (1:5000; Cell Signaling), nitrotyrosine (1:500; Cell Signaling), or GAPDH (1:2000; Santa Cruz Biotechnology, Santa Cruz, CA). Membranes were

then labeled with horseradish peroxidase–conjugated secondary antibodies. Immunoreactive bands were visualized using the ECL detecting reagent (GE Healthcare UK Ltd, Buckinghamshire, UK) and documented with an LAS 1000 (Fuji Photo Film, Kanagawa, Japan).

Data Analyses

The data presented as bar graphs are the means ± SDs in all experiments. Statistical analyses were performed using the Student's *t*-test, and $P < 0.05$ indicated statistical significance.

Results

Characterization of the Cygb$^{-/-}$ *Mice*

Cygb-deficient mice were generated by deleting exon 1 of the mouse *Cygb* gene (Figure 1A) and backcrossed on the C57BL/6J background. Southern blotting (Figure 1B) and PCR genotyping using mouse tail DNA (data not shown) confirmed the deletion of the *Cygb* gene. Both Cygb mRNA and protein expression were absent in *Cygb*$^{-/-}$ mouse livers, compared with wild-type livers (Figure 1C). Furthermore, IHC indicated that the Cygb protein was present in sinusoidal lining cells in addition to perivascular cells around the portal and central veins, as previously reported,[1] in *Cygb*$^{+/+}$ mice, whereas it was undetected in *Cygb*$^{-/-}$ mice (Figure 1D). Together, these data demonstrate the successful production of the *Cygb*$^{-/-}$ mice.

The mice homozygous for the disrupted allele appeared normal both morphologically and histopathologically 1 month after birth. Next, we examined whether Cygb influenced the toxicity and carcinogenesis of DEN in mice.

Cygb Deficiency Strongly Promotes DEN-Induced Tumorigenesis

DEN is a commonly used chemical carcinogen for the liver because it is activated by cytochrome P-450 enzymes in hepatocytes.[21] C57BL/6J mice were reported to be relatively resistant to liver tumor development under DEN treat-

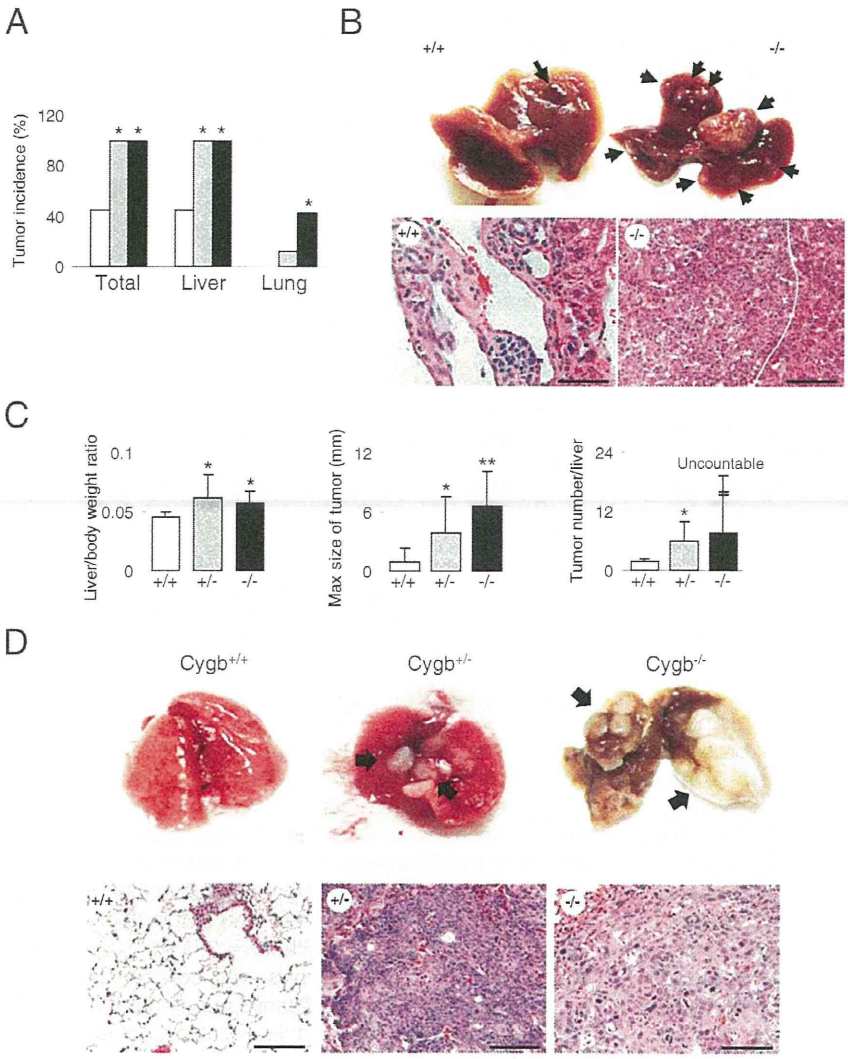

Figure 2. Tumor development in *Cygb*-deficient mice treated with 25-ppm DEN for 25 weeks. **A:** Tumor incidence in total, livers, and lungs from DEN-treated *Cygb*$^{+/+}$ (white bars), *Cygb*$^{+/-}$ (gray bars), and *Cygb*$^{-/-}$ (black bars) mice ($n = 7$ to 12). $^{*}P < 0.05$ compared with wild type. **B:** Representative gross photographs of livers (**top**) from wild-type (+/+) and *Cygb*-KO (−/−) mice treated with DEN. There was a marked increase in tumor multiplicity in *Cygb*-deficient mice compared with wild-type mice (**arrows**). Representative H&E-stained paraffin sections (**bottom**) of hemangioma from wild-type and poorly differentiated hepatocellular carcinoma composed of small immature neoplastic cells with mitotic figures (the line indicates the boundary of tumor and nontumor areas), from *Cygb*$^{-/-}$ mice. Scale bar = 100 μm. **C:** Determination of liver/body weight ratios, maximum (Max) tumor sizes, and liver tumor numbers for *Cygb*$^{+/+}$ (white bars), *Cygb*$^{+/-}$ (gray bars), and *Cygb*$^{-/-}$ (black bars) mice ($n = 7$ to 12). Values are given as the mean ± SD. $^{*}P < 0.05$, $^{**}P < 0.01$. **D:** Representative gross photographs (**top**) and microphotographs (**bottom**) of lungs from *Cygb*$^{+/+}$, *Cygb*$^{+/-}$, and *Cygb*$^{-/-}$ DEN-treated mice. Lung tumors were only found in *Cygb*$^{+/-}$ and *Cygb*$^{-/-}$ mice. **Arrows** indicate lung tumors that were classified as squamous cell carcinomas. Scale bar = 100 μm.

ment.[22,23] In this study, we examined whether the loss of Cygb could influence the toxicity and carcinogenesis of DEN in the tumor-resistant C57BL/6J strain. We administered 25-ppm DEN to the drinking water of *Cygb*-deficient male mice at the age of 4 weeks. Unexpectedly, as early as 25 weeks after DEN treatment, 100% of $Cygb^{-/-}$ and $Cygb^{+/-}$ mice developed tumors in the liver and lungs, whereas the tumor incidence in wild-type mice was 44.4% (Figure 2, A and B). The liver/body weight ratio was approximately 50% more than in wild-type animals (Figure 2C) because of these tumor masses. $Cygb^{-/-}$ mice displayed significantly larger lesions and produced tumors more frequently than wild-type mice (Figure 2C).

DEN has induced tumors in the liver and in the lungs of the B6C3F1 mouse strain, although with a lower frequency.[24] Consistent with these studies, lung tumors were found in $Cygb^{+/-}$ and $Cygb^{-/-}$ mice, with a frequency of 11.7% and 57.1%, respectively, whereas $Cygb^{+/+}$ mice showed complete resistance (Figure 2, A and D).

Next, using a low dose of DEN, at which wild-type mice do not develop liver tumors, we examined whether *Cygb* deficiency functioned as a tumor promoter. We took advantage of earlier observations that, when DEN was administered to mice at a nontoxic dose, it failed to induce liver cancer, unless combined with a tumor promoter, such as phenobarbital.[25,26] We maintained wild-type and *Cygb*-deficient male mice during DEN administration at the nontoxic dose of 0.05 ppm for 36 weeks. As a result, >40% of $Cygb^{-/-}$ mice developed tumors in the liver or lungs, whereas, as expected, wild-type mice exhibited no tumor formation (Figure 3). $Cygb^{+/-}$ mice showed an intermediate sensitivity. These findings confirm the tumor-promoting effects of *Cygb* depletion.

To define the histological features of the liver tumors, liver samples were evaluated IHC. The liver tumors in C57BL/6 mice (wild type) administered DEN in drinking water were dominantly composed of cholangiomas, hemangiomas, hemangiosarcomas, and, to a lesser degree, hepatocellular carcinomas.[27–29] In this study, *Cygb*-deficient and wild-type mice developed similar histological alterations in the liver, including hemangioma (Figure 2B), hepatocellular carcinoma (Figures 2B and 3B), which stained positive for alpha-fetoprotein (AFP) (Figure 4A), and cholangioma, which stained positive for CK19 (Figure 4A). Quantitative real-time PCR (RT-qPCR) analysis showed increased mRNA expression of AFP in $Cygb^{+/-}$ and $Cygb^{-/-}$ mice compared with their wild-type counterparts (Figure 4B).

In the liver, Cygb was present in stellate cells.[1,4] We used cellular retinol-binding protein-1 and α-smooth muscle actin antibodies to detect stellate cell expression. The presence of cellular retinol-binding protein-1– and α-smooth muscle actin–expressing cells in the liver parenchyma from DEN-treated homozygote mice indicated that stellate cells were present along sinusoids, even in the absence of Cygb (Figure 4C). The expression of α-smooth muscle actin and desmin, another marker of stellate cells, was markedly augmented in $Cygb^{-/-}$ mice (Figure 4C). Next, we assessed whether liver fibrosis developed in these mice. Sirius red staining for collagen deposition in paraffin-embedded sections of liver samples

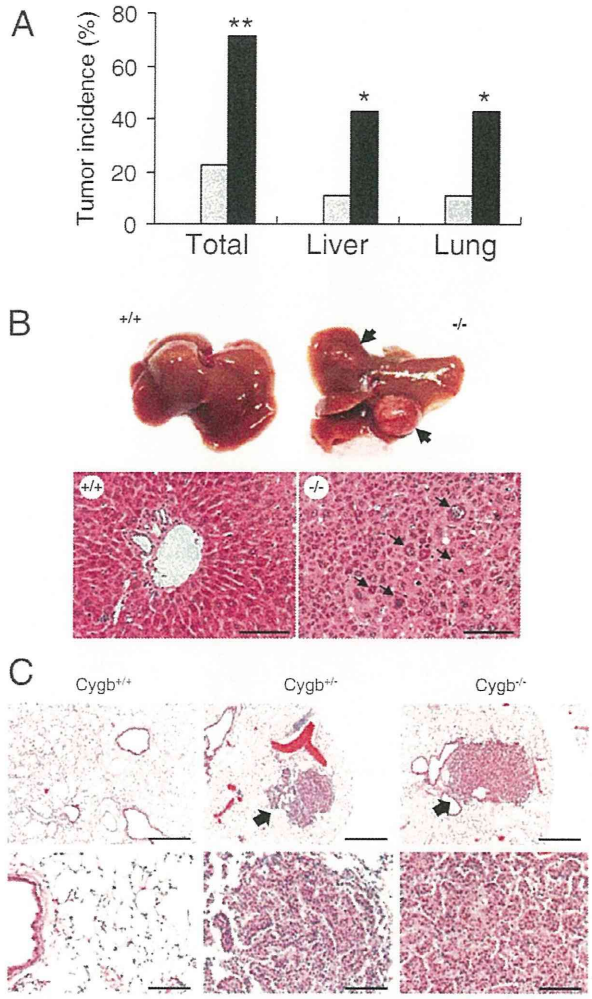

Figure 3. Tumor development in *Cygb*-deficient mice treated with 0.05-ppm DEN for 36 weeks. **A:** Tumor incidence in total, livers, and lungs from 0.05-ppm DEN-treated $Cygb^{+/+}$ (white bars), $Cygb^{+/-}$ (gray bars), and $Cygb^{-/-}$ (black bars) mice (n = 7 to 15). $^{*}P < 0.05$, $^{**}P < 0.01$ compared with the wild type. **B:** Gross photographs of livers (**top**) from $Cygb^{+/+}$ and $Cygb^{-/-}$ mice treated with 0.05-ppm DEN, as previously mentioned; **arrows** indicate lung tumors. Representative photomicrographs of H&E-stained paraffin sections of liver parenchyma (**bottom**) from wild-type and moderately differentiated hepatocellular carcinoma composed of large cells that vary in size and shape (**arrows**), from $Cygb^{-/-}$ mice. Scale bar = 100 μm. **C:** Representative photomicrographs of H&E-stained paraffin sections of lungs from $Cygb^{+/+}$, $Cygb^{+/-}$, and $Cygb^{-/-}$ mice treated with 0.05-ppm DEN for 36 weeks. Scale bars: 400 μm (**top**); 100 μm (**bottom**). **Arrows** indicate lung tumors that were classified as adenocarcinomas. No lung tumor was observed in $Cygb^{+/+}$ mice.

collected from $Cygb^{+/+}$ and $Cygb^{-/-}$ mice treated with 25-ppm DEN for 25 weeks showed marked deposition of collagen (red) around the hepatocytes (pericellular fibrosis) in $Cygb^{-/-}$ mice (Figure 4D). Morphometric image analysis was performed with a computerized system, consisting of a photomicroscope, a digital camera, and LuminaVision 2.4 bioimaging software, to quantitatively assess fibrosis. The Sirius red–positive area of $Cygb^{-/-}$ mice (7.67% ± 7.82%, n = 3) was significantly greater than that in $Cygb^{+/+}$ mice (mean ± SD, 1.36% ± 0.36%, n = 3; $P < 0.05$, Kruskal-Wallis test). Pericellular fibrosis with collagen deposition was accompanied by significantly augmented mRNA expression of collagen 1α1 and tissue inhibitor of matrix met-

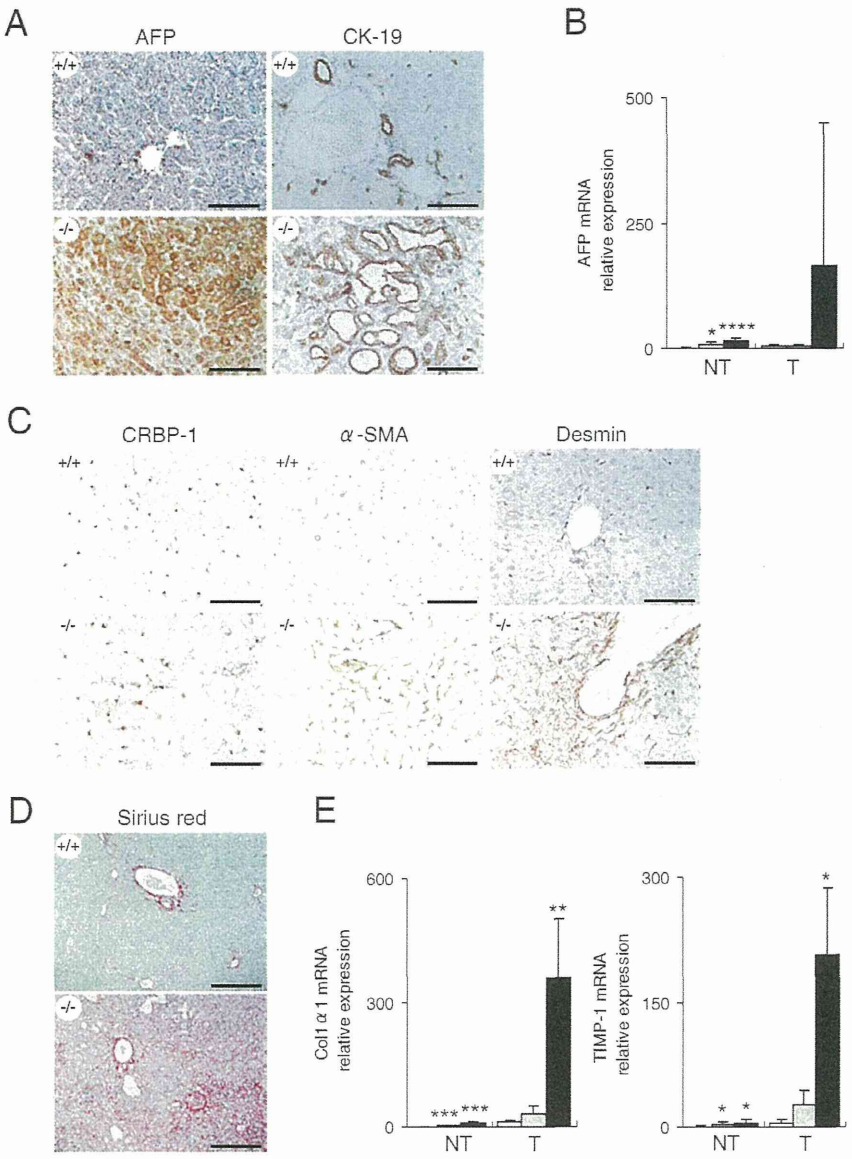

Figure 4. Expression of tumor markers and liver fibrosis development in DEN-treated *Cygb*-deficient mice. *Cygb*-deficient mice from Figure 2 were subjected to histological and biochemical analyses. **A:** Paraffin-embedded liver sections from $Cygb^{+/+}$ and $Cygb^{-/-}$ mice were stained with AFP and cytokeratin 19 (CK-19). Scale bar = 100 μm. **B:** Expression of AFP mRNA in $Cygb^{-/+}$ (white bars), $Cygb^{+/-}$ (gray bars), and $Cygb^{-/-}$ (black bars) mice livers was determined by RT-qPCR (n = 7 to 12). Levels were normalized to GAPDH. Values are given as the mean ± SD of all experiments. NT, nontumor area; T, liver tumor. $^{*}P < 0.05$, $^{****}P < 0.0001$. **C:** Paraffin-embedded liver sections were IHC stained for the detection of CRBP-1, α-SMA, and desmin. Scale bar = 100 μm. **D** and **E:** Development of liver fibrosis. **D:** Sirius red staining for collagen deposition in paraffin-embedded liver sections. Scale bar = 100 μm. There was marked deposition of collagen (red) around the hepatocytes (pericellular fibrosis) in $Cygb^{-/-}$ mice. **E:** Relative levels of collagen (Col) 1α1 and tissue inhibitor of matrix metalloproteinase-1 (TIMP-1) mRNA in the nontumor area (NT; n = 7 to 12) and in liver tumors (T; n = 3 to 5) of $Cygb^{+/+}$ (white bars), $Cygb^{-/-}$ (gray bars), and $Cygb^{-/-}$ (black bars) mice were determined by RT-qPCR and normalized to GAPDH mRNA. Values are given as the mean ± SD of all experiments. $^{*}P < 0.05$, $^{**}P < 0.01$, and $^{***}P < 0.001$.

taloproteinase-1 in the livers of $Cygb^{-/-}$ mice, compared with that of $Cygb^{+/+}$ mice treated with 25-ppm DEN for 25 weeks (Figure 4E). Thus, the augmented occurrence of pericellular fibrosis and fibrotic reactions in *Cygb* deficiency may be involved in the development of liver cancer.

Cygb *Loss Is Associated with Increased Cancer Cell Proliferation*

Two important cellular processes in tumorigenesis are cell apoptosis and proliferation. To examine how *Cygb* loss affected these two processes in the livers of C57BL/6J mice, we determined the labeling indexes of TUNEL, as a marker of apoptotic cells, and proliferating cell nuclear antigen (PCNA), as a marker of proliferating cells in the liver, both in the tumor and adjacent nontumor areas of $Cygb^{+/+}$ and $Cygb^{-/-}$ mice treated with 25-ppm DEN in drinking water for 25 weeks. Liver tumors in $Cygb^{-/-}$ mice exhibited reduced apoptotic cell death relative to liver tumors in $Cygb^{+/+}$ mice (Figure 5, A and C) and showed elevated mRNA expression of the antiapoptotic protein Bcl-2 (Figure 5E). Liver tumors in the $Cygb^{-/-}$ mice exhibited more proliferating cells than the tumors of the wild-type mice, as shown by PCNA labeling (Figure 5, B and D), in addition to elevated cyclin D1 mRNA expression (Figure 5F). These results suggest that stimulation of proliferating neoplastic cells is the primary cellular mechanism for increased liver tumorigenesis in *Cygb*-deficient mice.

Cygb-*Deficient Mice Exhibit Elevated Phosphorylated Akt and Erk and Liver Inflammation*

To identify the signaling pathways responsible for enhanced hepatocyte survival and proliferation, we ex-